PAPER

Check for updates

Bright and stable gold nanocluster assemblies by silica/zirconia double-shell encapsulation†

Shaochen Zhou, [ID] [a] Yanyan Duan, [ID] [b] Kai Liu [ID] [a] and Robin H. A. Ras [ID] *[ac]

Ultrasmall gold nanoclusters are fascinating fluorescent materials with many unique properties, yet, to render them highly luminescent and stable remains challenging. In this work, solvent-induced aggregates of gold nanoclusters are encapsulated in silica/zirconia nanostructures, realizing a significantly enhanced photoluminescence efficiency and stability. These silica and zirconia coated gold nanocluster aggregates achieved a photoluminescence quantum yield of ~55%, with high resistance to photobleaching and water, due to the stabilization by the dual-oxide matrix. Furthermore, we demonstrate their suitability for visualizing latent fingerprints.

1. Introduction

Metal nanoclusters, composed of several to dozens of atoms, emerge as promising fluorescent materials for bio/chemoanalysis,[1,2] and energy[3] and catalysis applications.[4,5] Fluorescent gold nanoclusters have attracted most of the scientific attention due to their superior performance compared to their silver and copper counterparts.[6–8] Various molecules or templates, such as amino acids,[9] peptides,[10] thiolates,[11,12] dendrimers[13] and macromolecules,[1,14] have been utilized as stabilizers to synthesize gold nanoclusters with different fluorescence properties in the past decades.

Nevertheless, gold nanoclusters (GNCs), like other fluorescent materials, suffer from stability problems. The ultrasmall size of GNCs results in extremely high surface activity, making them most susceptible to ambient environments. Prolonged exposure to light or heat could cause emission quenching of fluorescent GNCs. Diverse methods have been developed to improve the stability of metal nanoclusters, such as coating these ultra-small particles with protective shells,[15] confining them within stable substrates[16,17] and exchanging their surface ligands with robust stabilizers.[18]

Inert-shell coating is among the most effective ways to achieve superior stability.[19,20] The shell inhibits the encapsulated substances from structural destruction or chemical degradation. However, coating usually leads to an unwanted decrease in photoluminescence quantum yields (PLQYs), which is especially

unfavorable for fluorescent metal nanoclusters. Although highly luminescent metal nanoclusters (PLQY > 60%) have been reported in recent years,[21,22] PLQYs of most of the metal nanoclusters remain at less than 10%. Therefore, synthetic strategies to improve both the stability and PL efficiency of GNCs are still important.

Herein, we introduce silica and zirconia coated GNC aggregates (GNCAs), namely GNCA/SiO$_2$/ZrO$_2$ nanoparticles (NPs), with high stability and strong emission. The GNCAs exhibit strong PL due to the aggregation-induced emission enhancement (AIEE) effect, which can offset the PLQY decrease that coating could cause to the fluorophores.[23,24] However, the aggregates are extremely vulnerable to ambient conditions due to the weakly bonded structure. The outside silica–zirconia shell hereby provides a robust fixation and protection effect, leading to a significant improvement in stability. Being resistant to UV light and sensitive environments, GNCA/SiO$_2$/ZrO$_2$ NPs can achieve a PLQY of ~55%, showing potential for applications like illumination, displays and fluorescence analysis.

Detection of latent fingerprints (LFPs) has been extensively applied in identity recognition. However, the LFPs could be barely seen with the naked eye because of their low optical contrast. One effective technique is to adhere powder contrast agents to the LFPs to increase the overall visibility. Various contrast agents, such as conjugated oligomers[25,26] and magnetic particles,[27] have been developed to visualize LFPs. The highly emissive and stable GNCA/SiO$_2$/ZrO$_2$ NPs can also serve as a competent fluorescent contrast agent in LFP detection, in which both the oxide matrix and incorporated GNCAs play an important role. The dual-oxide shell increases the overall stability and provides a compatible surface (*e.g.*, fingerprint residue-affinitive), and the encapsulated GNCAs give out a strong PL that allows high-contrast imaging under UV light. Moreover, composed of low-toxicity constituents, GNCA/SiO$_2$/ZrO$_2$ NPs exhibit applicability in areas that require high biocompatibility.

[a] Department of Applied Physics, School of Science, Aalto University, FI-00076 Espoo, Finland. E-mail: robin.ras@aalto.fi

[b] IMDEA Materials Institute, Calle Eric Kandel 2, Getafe, 28906, Spain

[c] Department of Bioproducts and Biosystems, School of Chemical Engineering, Aalto University, FI-00076 Espoo, Finland

† Electronic supplementary information (ESI) available. See DOI: https://doi.org/10.1039/d2tc00824f

This journal is © The Royal Society of Chemistry 2022

J. Mater. Chem. C, 2022, **10**, 10001–10008 | **10001**

2. Experimental

2.1 Chemicals

Gold chloride (HAuCl$_4$·3H$_2$O, 99%), L-glutathione reduced (GSH, ≥98%), ammonium hydroxide aqueous solution (NH$_3$·H$_2$O, 28–30%), and tetraethyl orthosilicate (TEOS, 98%, reagent grade) were purchased from Sigma Aldrich. Dodecane (C$_{12}$H$_{26}$, 99%), zirconium(IV) *tert*-butoxide (ZTB, 99.999% trace metal basis), and polyvinylpyrrolidone (PVP, M.W. 10000) were obtained from Alfa Aesar. Ethanol (C$_2$H$_5$OH, 99.5%) was purchased from Altia Oyj (Finland). All the reagents were utilized without further purification. Millipore ultrapure water with a resistance of 18.2 MΩ was used throughout the work.

2.2 Synthesis of GNCs

Fluorescent gold nanoclusters are synthesized according to reported procedures.[10] 0.5 mL of HAuCl$_4$ aqueous solution (20 mM) is mixed with 4.35 mL of ultrapure water, followed by the addition of GSH aqueous solution (100 mM, 150 μL). The as-obtained solution is stirred at 20 °C for 15 min until it becomes colorless and transparent, which is then heated at 70 °C for another 24 h. Byproducts are removed after 12 h of dialysis to purify the as-obtained GNC solution, which is stored under 4 °C for subsequent use.

2.3 Synthesis of GNCA/SiO$_2$ NPs

GNCAs are encapsulated into silica matrices using a modified Stöber method. 1 mL of GNC solution is mixed with 9 mL of ethanol to form dense GNCAs, followed by the addition of 200 mg of PVP. The mixture is ultrasonicated at 37 kHz, 100 W for 10 min. Then, NH$_3$·H$_2$O solution (125 μL) is added into the system, followed by slow addition of TEOS (250 μL) to initiate the hydrolysis and condensation of silane. The system is stirred at 400 rpm, 20 °C for 72 h. The pale-yellow products are collected by centrifugation at 11 000 rpm for 10 min, followed by washing with ethanol to remove excess reactants and byproducts. The final products are obtained after three-time washing and calcination at 50 °C for 12 h.

2.4 Synthesis of GNCA/SiO$_2$/ZrO$_2$ NPs

Typically, 100 mg of the as-prepared GNCA/SiO$_2$ NPs are dispersed in 10 mL of dodecane after sonication at 37 kHz, 100 W for 20 min. 100 μL of ZTB is added into the dispersion, which is stirred without sealing at 400 rpm, 20 °C for 48 h. The hydrolysis and condensation of ZTB proceed spontaneously and consume the residual water in the air. The products are collected by centrifugation at 6000 rpm for 5 min, which are washed with ethanol three times. GNCA/SiO$_2$/ZrO$_2$ NPs are obtained after calcination at 50 °C for 12 h.

2.5 Characterization

Micromorphology is analyzed by high-resolution transmission electron microscopy (HR-TEM) and scanning electron microscopy (SEM), using a JEM 2800 HR-TEM and a JSF 7500FA high-resolution analytical SEM, respectively. HR-TEM is performed at an acceleration voltage of 200 kV. The samples for the TEM measurement are prepared by drop-casting on holey carbon copper grids. UV-vis absorption spectra are collected using a UV-vis-NIR Agilent Cary 5000 spectrophotometer. Fourier transmission infrared spectroscopy (FTIR) is performed using a Nicolet 380 FTIR spectrometer (Thermo Electron Corporation). Dynamic light scattering (DLS) analysis is carried out using a Malvern Zetasizer Nano-ZS90 instrument. Steady-state fluorescence spectroscopy is performed using a PTI QuantaMaster 40 fluorescence spectrometer. Time-resolved fluorescence spectroscopy and absolute photoluminescence quantum yield (PLQY) measurements are carried out with an FS5 Spectrofluorometer (Edinburgh Instruments). PLQYs are measured using the SC-30 module coupled with an integrating sphere, in which the powder or liquid samples are excited at 390 nm. The PL decay curves are collected and analyzed using a time correlation single photon counting (TCSPC) system. A picosecond pulsed diode laser (EPL-375, Edinburgh Instruments) with a pulse width of 64.3 ps and a wavelength of 377.6 nm is used for excitation.

2.6 Latent fingerprint detection

The latent human fingerprints are acquired by pressing for 5 s on clean substrates (glass, polystyrene and aluminum alloy). The GNCA/SiO$_2$/ZrO$_2$ powder is then introduced on the substrates to cover the imprinted area, which is quickly adhered to the LFPs. The excess powder is removed by a gentle N$_2$ gas flow. The pictures are taken by a phone camera under room light and UV light at 365 nm, respectively.

3. Results and discussion

3.1 Synthesis of GNCA/SiO$_2$/ZrO$_2$ NPs and their optical properties

3.1.1 Chemical synthesis of GNCA/SiO$_2$/ZrO$_2$ NPs.
Scheme 1 shows the synthesis of GNCA/SiO$_2$/ZrO$_2$ NPs, which undergoes three typical stages: (1) formation of PVP-stabilized GNCAs by a solvent-induced assembly process, (2) generation of silica coated GNCAs through hydrolysis and condensation of silane, and (3) formation of zirconia on the surface of GNCA/SiO$_2$ NPs.

The as-prepared GNCs are Au(0) clusters that are capped by Au(I)–glutathione oligomeric complexes, whose emission originates from charge transfer within their Au(I) rich surface.[10]
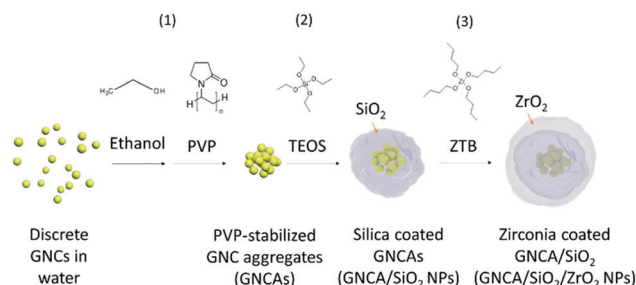
Scheme 1 Synthesis process of GNCA/SiO$_2$/ZrO$_2$ NPs. GNCAs are formed in the presence of excess ethanol and stabilized by PVP. GNCAs are first encapsulated into the silica matrix and further coated by zirconia through hydrolysis and condensation processes.

10002 | *J. Mater. Chem. C*, 2022, **10**, 10001–10008

This journal is © The Royal Society of Chemistry 2022

Reducing the distance between the GNCs will lead to a substantial increase in the fluorescence intensity because of the AIEE effect, which is effective in boosting the PL efficiency of various fluorescent metal nanoclusters.[28–30]

It is thermodynamically favorable for these polar GNCs to aggregate in the ethanol–water environment, due to the disruption of the hydration shell and charge neutralization of GNCs.[23] Fig. 1(a) shows the hydrodynamic diameter and relative PL intensity of the GNC water–ethanol mixture, which change with the volume fraction of ethanol. The hydrodynamic diameter of the dispersed phase increases from initial $\sim$2.5 nm to $\sim$262 nm as the volume fraction of ethanol increases to 50%, which indicates large aggregation of GNCs. The hydrodynamic diameter decreases further when more ethanol is present, reaching $\sim$134 nm when the volume of ethanol accounts for 90%. The PL emission also changes with the clustering of GNCs. Aggregation of GNCs leads to a constant increase in the emission intensity, as well as a blue shift in the peak wavelength. The emission intensity increases by 389%, and the peak blue-shifts from 603 nm to 589 nm (Fig. S1, ESI†) upon the formation of GNCAs (ethanol 90 v/v%). Clearly, the clustering of GNCs decreases the average inter-particle distance and gives rise to the AIEE effect.

PVP molecules are added to stabilize the nanocluster aggregates from precipitation by concentrating on the interface between the ethanol and GNC aqueous droplets because of their amphiphilic properties.[31] PVP not only keeps the GNCAs dispersed in ethanol, but also directs the hydrolysis and condensation of silane around the aggregates. GNCAs are thereby encapsulated in a SiO_2 matrix. It is noteworthy that the formation of silica not only provides a protective layer for the GNCAs, but also consumes most of the water molecules in the droplet, which is necessary for the subsequent zirconia coating. The ZrO_2 precursor, ZTB, is too water-sensitive to hydrolyze controllably in a water-rich environment. Thus, zirconia is deposited on the silica coated GNCAs in an oil phase. ZTB reacts with the ambient water and produces a ZrO_2 layer that covers the silica surface, producing GNCA/SiO_2/ZrO_2 NPs.

3.1.2 PL properties of GNCA/SiO_2/ZrO_2 NPs. Fig. 1(b) shows the normalized excitation and emission spectra of GNCA/SiO_2/ZrO_2 NPs and GNCs. They share almost the same excitation bands, while the emission band of GNCA/SiO_2/ZrO_2 NPs blue shifts by 14 nm to 589 nm with respect to 603 nm of GNCs, consistent with that of GNCAs. The PL decay curves indicate a longer average PL lifetime for GNCA/SiO_2/ZrO_2 NPs, which is 10.3 μs, in comparison with 3.7 μs of GNCs (Fig. 1(d)). Their micro-second lifetimes indicate that the emissions originate from the triplet excited states, which are associated with charge transfer behaviors between gold and the ligands.[32]

Fig. 1(c) shows the emission brightness comparison between GNCA/SiO_2/ZrO_2 NPs and GNCs. Both the emission spectra and inset picture reveal that GNCA/SiO_2/ZrO_2 NPs produce a much brighter emission than the GNCs do. GNCA/SiO_2/ZrO_2 NPs have an absolute PLQY of 54.79%, an approximately eleven-fold increase with respect to 4.76% of GNCs (Table S1, ESI†). It is noteworthy that coating could in principle lead to a decrease in the PLQY, when the outside layer could not only cause an emission energy loss, but also increase the light absorption.
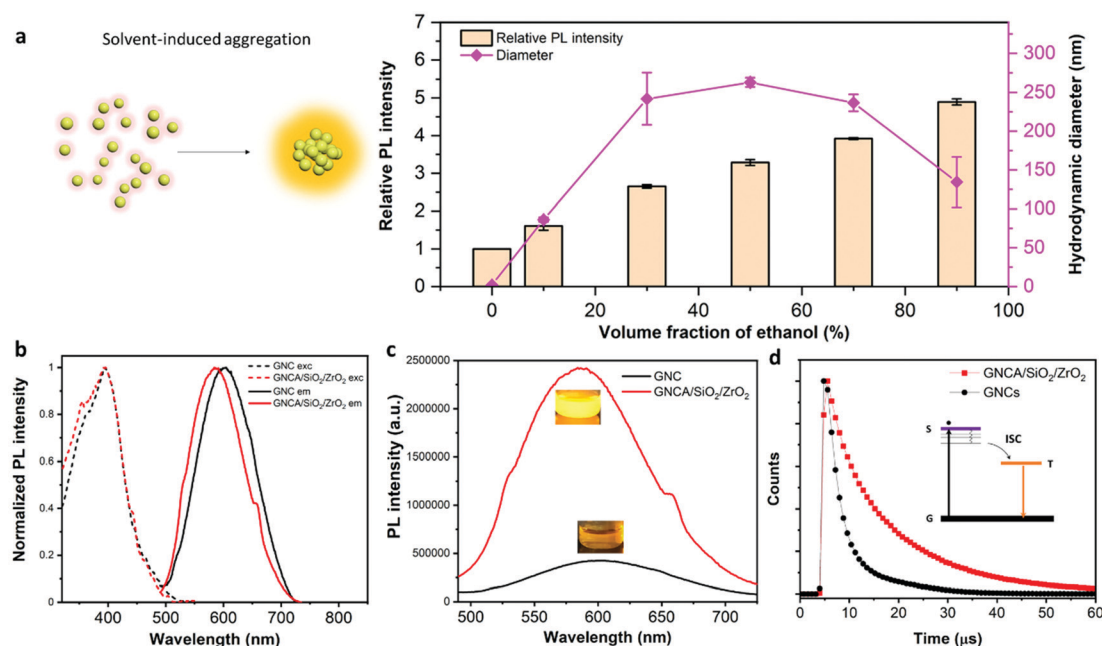

Fig. 1 (a) Left: illustration on the solvent-induced aggregation of GNCs with enhanced emission. Right: The hydrodynamic diameter and relative PL intensity of the GNC–water–ethanol mixture as a function of volume fraction of ethanol. Highly emissive GNCAs are formed when the volume fraction of ethanol reaches 90%. (b) and (c) Steady-state PL spectra of GNCs and GNCA/SiO_2/ZrO_2 NPs: the normalized excitation and emission spectra (b) and the absolute emission spectra (c). The molar concentration of Au for both GNCs and GNCA/SiO_2/ZrO_2 NPs is 1 mM. (d) Time-resolved PL spectra of GNCs and GNCA/SiO_2/ZrO_2 NPs. The average PL lifetimes are both on a microsecond scale.

This journal is © The Royal Society of Chemistry 2022

J. Mater. Chem. C, 2022, **10**, 10001–10008 | **10003**

In addition, the aggregation of fluorophores could also result in the loss of PL (aggregation-induced quenching), due to the depopulation of excitons.[33,34] Yet, in our work, we managed to offset these negative effects by taking advantage of the AIEE properties.

The AIEE origin of the glutathione-capped metal nanoclusters has been discussed in recent studies.[10,35,36] Structure rigidification is one of the major causes for the conspicuous emission enhancement.[21] In this work, GNCAs in the oxide matrixes are most likely affected by the structure rigidification triggered by aggregation and matrix encapsulation, because of which the non-irradiative recombinations are greatly inhibited.

As discussed above, the PL of GNCs stems from the radiative ligand–metal charge transfers. The ligand–metal charge transfer would go through non-radiative pathways when there are fierce thermal motions, including the nanocluster movement and ligand fluctuation, to meet the demand for thermal energy. The thermal motions decrease the PLQYs and PL lifetimes of GNCs profoundly, since fewer excitons go through the radiative pathway for the recombination.[21,37] This can be partially manifested by the significantly stronger PL intensities of GNCs and GNCA/SiO$_2$/ZrO$_2$ NPs at low temperatures (Fig. S2 and S3, ESI†).

The aggregation extent and the encapsulation in the oxide matrixes provide a quite rigid medium for every encapsulated GNC. The GNCs are sterically confined, and their surface ligands are given little freedom for rotation, fluctuation, and other thermal energy-consuming motions. The fewer thermal motions, the fewer non-radiative ligand–metal charge transfers. Therefore, more excitons are going through the radiative pathways for the recombination, increasing the PLQYs and the PL lifetimes. This explains the great PL performance enhancement that is observed in GNCA/SiO$_2$/ZrO$_2$ NPs as compared to that of GNCs.

3.2 Morphology, composition and structure

3.2.1 Morphology. The solid GNCA/SiO$_2$/ZrO$_2$ NPs appear as yellowish white powder, which emit bright orange emission upon UV excitation (365 nm, Fig. 2(a)). SEM images in Fig. 2(b) and Fig. S4 (ESI†) reveal the surface morphology of GNCA/SiO$_2$/ZrO$_2$ NPs on a microscopic scale. Spherical oxide particles with rough surfaces and dimensions of 50–250 nm can be observed. The sizes of these particles are highly dependent on the dimension of encapsulated GNCAs. The STEM images exhibit more information on the inner morphology of GNCA/SiO$_2$/ZrO$_2$ NPs (Fig. 2(c) and Fig. S5, ESI†). It can be seen that clusters of ultrasmall particles, namely GNCAs, are well coated by the amorphous shell. The spherical nanocluster aggregates are sized from 51 to 145 nm, smaller than the DLS results revealed in Fig. 1(a) (98–172 nm), due to the elimination of the hydration shell after the silica coating. This result also suggests that PVP, the stabilizer of the GNCAs, has successfully directed the formation of the oxide shell to encapsulate the spherical aggregates. An insufficient amount of PVP will lead to a structural disruption of the nanocluster aggregates and highly interconnected products (Fig. S6, ESI†). The average diameter of GNCs in the oxide matrix is ∼1.8 nm, while discrete GNCs

have a size of ∼1.7 nm (Fig. S7, ESI†), indicating that GNCs have not experienced apparent changes after the oxide coating.

3.2.2 Composition and structure. Fig. 2(d) shows the EDX spectrum of the GNCA/SiO$_2$/ZrO$_2$ particle. The presence of S, Au, Zr, Si and O is observed in the scanned area, indicating that GNCs, zirconia and silica make up the material. The structure of GNCA/SiO$_2$/ZrO$_2$ NPs is further revealed by X-ray mapping analysis (Fig. 2(e) and Fig. S8, ESI†). Fig. S8 (ESI†) shows the elemental distributions of S, Si and Zr on the GNCA/SiO$_2$/ZrO$_2$ particle, which represent GNCs, silica and zirconia layer, respectively (due to the close characteristic energy with Zr, Au is not selected as the typical element for GNCs). The S element, which comes from the surface ligands of GNCs, is concentrated in the nanocluster aggregates. While overlapping, the distributions of S and Si elements results in an apparent core/shell structure, suggesting the encapsulation of GNCAs in the silica matrix. A further distribution overlap of S, Si and Zr elements confirms the outmost zirconia shell. Clearly, as revealed in Fig. 2(e), the GNCA/SiO$_2$/ZrO$_2$ NPs have a typical core/shell/shell structure: aggregates of GNCs are capped by an inner silica shell and an outer zirconia layer.

Fig. 2(f) shows the UV-vis absorption spectra of GNCs, GNCA/SiO$_2$ NPs and GNCA/SiO$_2$/ZrO$_2$ NPs. Compared with GNCs, GNCA/SiO$_2$ NPs show a dominant feature of silica. The characteristic absorption peak of GNCs at 396 nm[10] becomes inconspicuous in the absorption spectrum of GNCA/SiO$_2$ NPs. But the absorption peak at 223 nm, the characteristic of SiO$_2$,[38] is intense. The spectrum of GNCA/SiO$_2$/ZrO$_2$ NPs shows other apparent absorption peaks at 237 nm and 309 nm, which are assigned to ZrO$_2$,[39] besides the peak at 223 nm for the SiO$_2$ component. This result further confirms the dual-oxide feature of GNCA/SiO$_2$/ZrO$_2$ NPs. Plasmonic absorption peaks at 500–550 nm for plasmonic gold NPs are absent in all the spectra, demonstrating that no larger gold particles have been formed after the silica and zirconia coating.

Fig. 2(g) shows the FTIR spectra of GNCs, GNCA/SiO$_2$ NPs and GNCA/SiO$_2$/ZrO$_2$ NPs. It should be noted that the spectrum of GNCA/SiO$_2$/ZrO$_2$ NPs is quite similar to that of GNCA/SiO$_2$ NPs, but different from that of GNCs, since most of the transmittance peaks stemming from the SiO$_2$ component. The peak at 1071 cm^{-1} is ascribed to the asymmetric stretching vibration of Si–O–Si, a typical bond in silica. The peaks at 553 and 502 cm^{-1} are assigned to the stretching vibration of Zr–O,[40] a typical bond in zirconia. It is worth mentioning that the characteristic peaks of Zr–O bonds are concentrated in the range of 400–800 cm^{-1}. As a result, the transmittance band of GNCA/SiO$_2$/ZrO$_2$ NPs exhibits a stronger intensity than that of GNCA/SiO$_2$ NPs in this wavenumber range (Fig. S9, ESI†). In general, all the spectral results indicate that the GNCAs are well encapsulated in the SiO$_2$/ZrO$_2$ matrix.

3.3 Stability evaluation

Stability is of great significance to practical applications for fluorescent metal nanoclusters. Fig. 3 reveals the emission changes of GNCA/SiO$_2$/ZrO$_2$ NPs under different conditions, such as exposure to water and UV light. The higher resistance to

10004 | *J. Mater. Chem. C*, 2022, **10**, 10001–10008

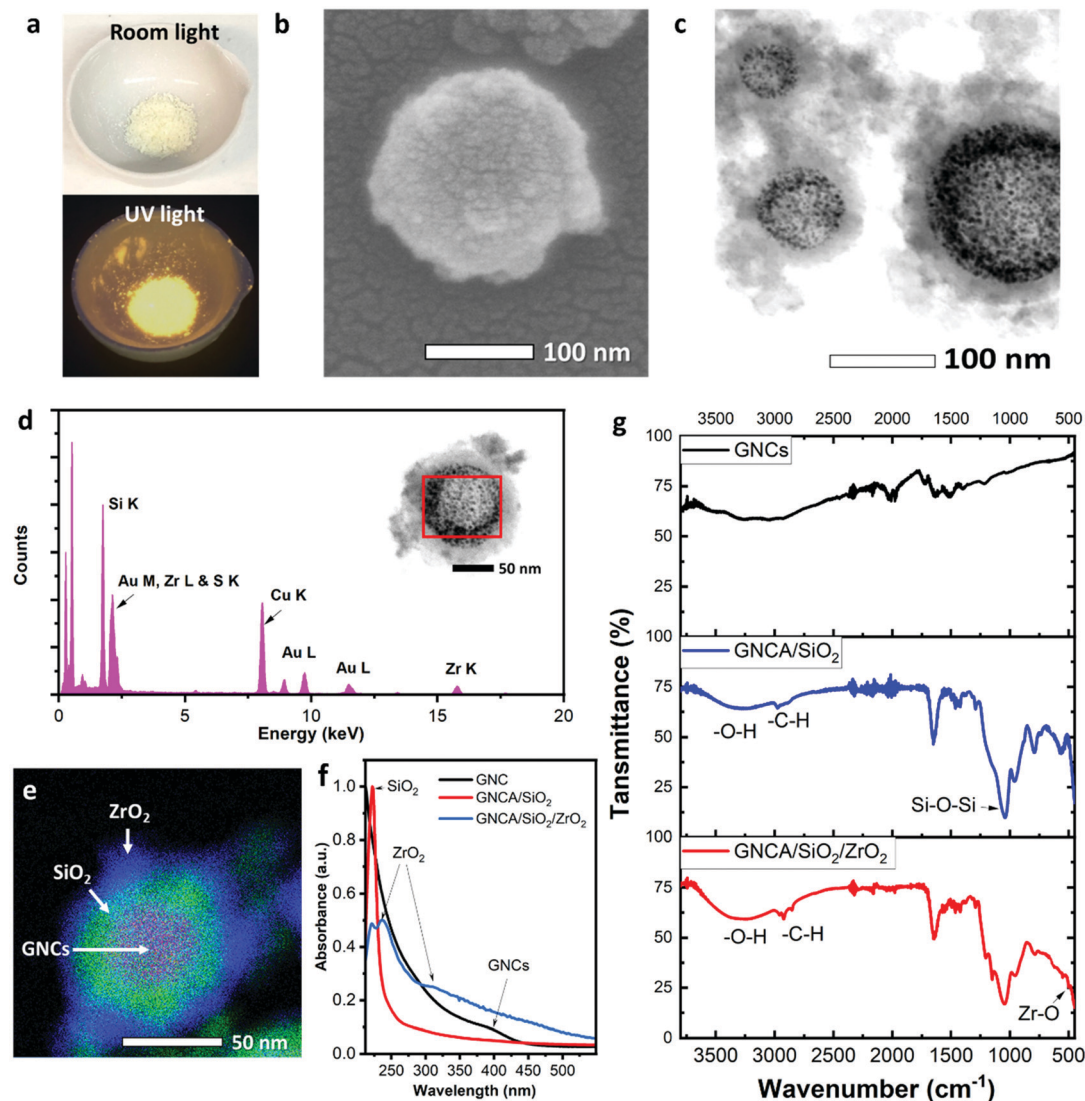This journal is © The Royal Society of Chemistry 2022

Fig. 2 Morphology, structure and composition of GNCA/SiO₂/ZrO₂ NPs. (a) Photographs of GNCA/SiO₂/ZrO₂ NPs under room light (up) and UV light at 365 nm (down). The yellowish white powder exhibits bright fluorescence under excitation at 365 nm. (b) SEM image of GNCA/SiO₂/ZrO₂ NPs. (c) Bright-field STEM image of GNCA/SiO₂/ZrO₂ NPs. The nanocluster aggregates are well incorporated in the oxide matrix. (d) EDX spectra (area scan) of the GNCA/SiO₂/ZrO₂ NP. Si, Zr, Au and S can be observed. Inset: STEM image of the GNCA/SiO₂/ZrO₂ NP in the bright field mode. (e) X-ray mapping result of a typical GNCA/SiO₂/ZrO₂ particle: distributions of Zr from ZrO₂ (blue), Si from SiO₂ (green) and S from GNCs (purple) suggest a GNC core/SiO₂ shell/ZrO₂ shell structure. (f) and (g) UV-vis absorption (f) and FTIR (g) spectra of GNCs, GNCA/SiO₂ NPs and GNCA/SiO₂/ZrO₂ NPs, respectively.

PL changes indicates a better stability for the GNCAs in the dual-oxide matrix.

3.3.1 Hydrostability. Resistance to water becomes indispensable for GNCA/SiO₂/ZrO₂ NPs due to the hydrophilicity of GNCAs. The nanocluster aggregates are highly water-sensitive because GNCs are extremely prone to separation, rather than staying together, in the water-rich environment (Fig. S10, ESI†). The collapse of aggregates will result in a sharp decrease in the emission intensity, due to the failure of the AIEE effect. Fig. 3(a) and (b) display the PL spectra of GNCA/SiO₂ NPs and GNCA/SiO₂/ZrO₂ NPs when they are dispersed in water and ethanol to form suspensions, respectively. A PL intensity decrease by ∼53% occurs on GNCA/SiO₂ NPs when they are dispersed in water. It is likely because the silica shell has pores or holes on

the surface,[23] allowing water molecules to diffuse through the matrix. The emission band is broadened when GNCA/SiO₂ NPs are dispersed in water (Fig. 3(a) inset), which suggests an increased proportion of the weak emission (λ_{em} = 603 nm) that GNCs emit in water. The silica shell becomes less rigid for GNCs when the water molecules diffuse into the matrix, which means a less effective inhibition of the ligand motions, resulting in a great intensity decrease. On the other hand, dispersion of GNCA/SiO₂/ZrO₂ NPs in water only causes the intensity to decrease slightly by ∼3%, demonstrating an enhanced water-resistant performance.

Fig. 3(c) shows the relative PL intensity change of GNCA/SiO₂ NPs and GNCA/SiO₂/ZrO₂ NPs in water to reveal their sustainability in water resistance. The emission intensity of GNCA/SiO₂
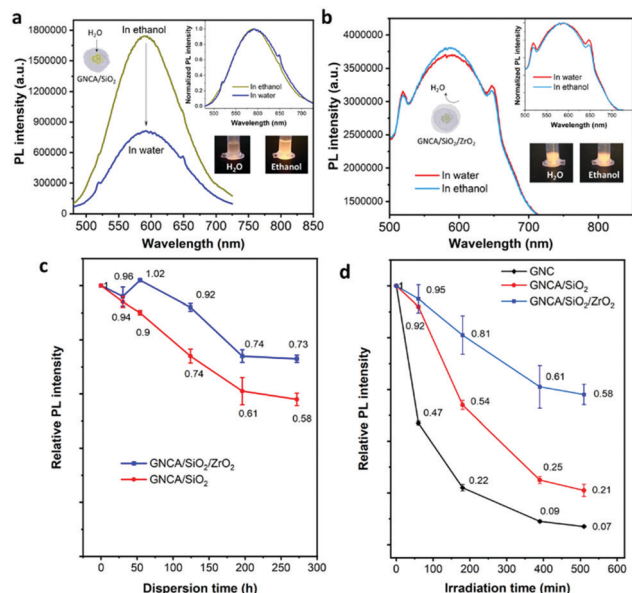
Fig. 3 Hydro- and photo-stability evaluation. (a) and (b) PL spectra of GNCA/SiO$_2$ NPs (a) and GNCA/SiO$_2$/ZrO$_2$ NPs (b) in water and ethanol. Inset figures: Normalized PL spectra of GNCA/SiO$_2$ NPs (a) and GNCA/SiO$_2$/ZrO$_2$ NPs (b) in water and ethanol. Inset photographs: Dispersions of GNCA/SiO$_2$ NPs (a) and GNCA/SiO$_2$/ZrO$_2$ NPs (b) in water and ethanol. (c) PL evolution of GNCA/SiO$_2$ NPs (red) and GNCA/SiO$_2$/ZrO$_2$ NPs (blue) under dispersion in water at 293 K over time. (d) PL evolution of GNCs (black), GNCA/SiO$_2$ NPs (red) and GNCA/SiO$_2$/ZrO$_2$ NPs (blue) in ethanol over time under UV irradiation at 350 nm, 5.96 mW cm^{-2}.

NPs shows a gradual decrease in the intensity, which is ∼58% of the initial value after dispersion for 272 h. However, the emission intensity of GNCA/SiO$_2$/ZrO$_2$ NPs decreases more slowly in the first 124 h, which decreases by only ∼8% and remains at ∼73% of the initial value after 272 h in water. These results indicate better hydrostability for GNCA/SiO$_2$/ZrO$_2$ NPs as compared to that of GNCA/SiO$_2$ NPs. It is the SiO$_2$/ZrO$_2$ shell that keeps most of the water molecules away, and maintains the aggregates from collapsing to discrete, weakly emissive GNCs.

3.3.2 Photostability. Photostability is highly important for fluorophores because of their frequent exposure to light excitation. Their fluorescence can be easily quenched by irreversible photo-induced reactions. Fig. 3(d) shows the relative PL intensity changes of GNCs, GNCA/SiO$_2$ NPs and GNCA/SiO$_2$/ZrO$_2$ NPs under continuous UV irradiation (350 nm, 6 mW cm^{-2}). The high-intensity UV light quickly quenches the PL of GNCs, whose intensity decreases by ∼53% in the first 60 min and remains only at ∼7% of the initial value after 510 min irradiation. However, GNCA/SiO$_2$ NPs, under the stabilization of the silica shell, show a slower quenching rate. Their residual PL intensity remains at ∼21% of the initial value after irradiation for the same period. However, it is noteworthy that a thicker silica shell does not lead to an improvement in photostability (Fig. S11 and Table S2, ESI†), largely because the shell is not dense enough to prevent the penetration of ambient active species.

A secondary coating with zirconia can improve the photostability conspicuously. The emission intensity of GNCA/SiO$_2$/ZrO$_2$ NPs remains at *ca.* 60% of the initial value after 510 min

under high-intensity UV light, significantly higher than those of GNCs and GNCA/SiO$_2$ NPs. Obviously, the SiO$_2$/ZrO$_2$ shell is more effective in inhibiting the unwanted photochemical reactions by both preventing active species (*e.g.*, photo-generated free radicals) and prohibiting the mobility of GNCs. Varying the amount of zirconia results in a significant change in photostability: more zirconia leads to a better UV resistance (Fig. S11 and Table S2, ESI†). These results suggest the indispensability of ZrO$_2$ in the photostability improvement.

3.4 Latent fingerprint detection

As shown in Fig. 4, GNCA/SiO$_2$/ZrO$_2$ NPs can be applied as an effective contrast agent in imaging the LFPs, which cannot be easily found on many surfaces due to the low-optical contrast. Detection of LFPs requires a strong adhesion between the contrast agent and fingerprint residues to achieve an easy visualization. Besides, a significant PLQY is also necessary to ensure a clear, emissive fingerprint pattern for detailed recognition under light excitation. Composed of highly luminescent GNCAs and the fingerprint residue-affinitive oxide shell, GNCA/SiO$_2$/ZrO$_2$ NPs show promise in LFP detection. Fig. 4(b) and (c) display the photographs of a LFP on the glass substrate before and after adhesion by the GNCA/SiO$_2$/ZrO$_2$ NPs. The fingerprint is almost invisible on the transparent substrate, which emerges after adhesion by the GNCA/SiO$_2$/ZrO$_2$ powder. Fingerprint details, such as ridge flows and ridge orientation field, can be clearly seen under visible light (Fig. 4(c)). The fingerprint becomes even clearer under UV excitation, as a result of a larger contrast between the emissive pattern and the dark background (Fig. 4(d)). Fig. 4(e$_1$)–(e3) reveal more morphological details. A ridge ending, a bifurcation and an island can be observed in the marked areas. And a right loop pattern can be found in the core area of the fingerprint. All the morphological details developed by the GNCA/SiO$_2$/ZrO$_2$ powder provide sufficient information for fingerprint type classification and indexing.[41]

More substrates are used to investigate the compatibility of the GNCA/SiO$_2$/ZrO$_2$ powder in LFP detection. A transparent, hydrophobic polystyrene cover and a hydrophilic aluminum alloy plate are selected as the typical substrates with different hydrophilicities and transparency. As shown in Fig. 4(f) and (g), LFPs on these substrates can be easily visualized by the GNCA/SiO$_2$/ZrO$_2$ powder, demonstrating good compatibility with various substrates.

Interestingly, the LFP patterns developed by GNCA/SiO$_2$/ZrO$_2$ NPs exhibit better storage stability than those by GNCA/SiO$_2$ NPs. As shown in Fig. 4(h), the pattern developed by GNCA/SiO$_2$ NPs gives out a greatly quenched PL after a seven-day storage in the dark environment (temperature: 21 °C; relative humidity: 80%). As a result, the background interference becomes strong, increasing the difficulty in further analysis. However, the emissive pattern developed by GNCA/SiO$_2$/ZrO$_2$ NPs shows little change after 7 days (Fig. 4(i)), suggesting better resistance to the ambient environment. A denser SiO$_2$/ZrO$_2$ shell is responsible for the stability difference between GNCA/SiO$_2$/ZrO$_2$ NPs and GNCA/SiO$_2$ NPs.

10006 | *J. Mater. Chem. C*, 2022, **10**, 10001–10008

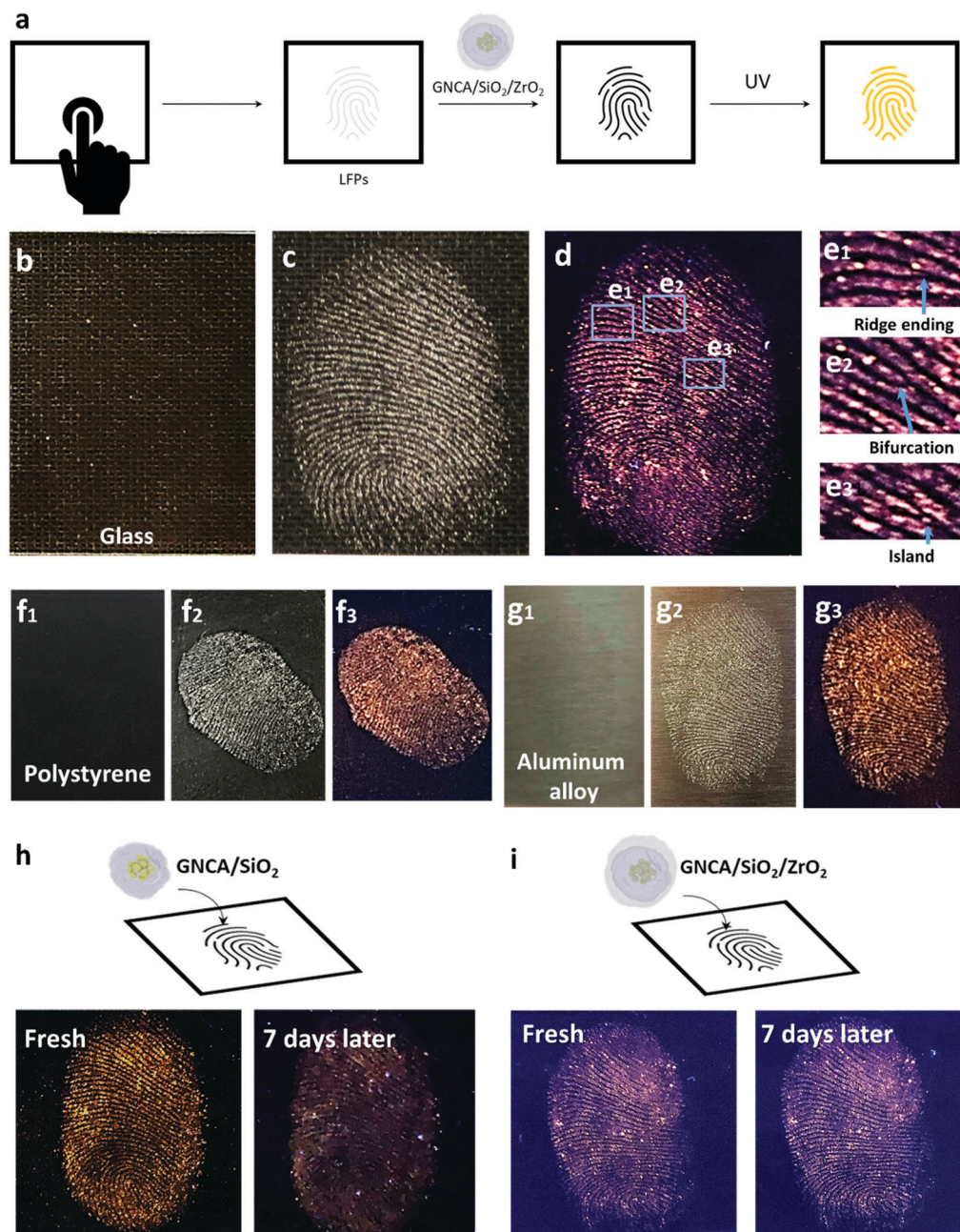This journal is © The Royal Society of Chemistry 2022

Fig. 4   GNCA/SiO$_2$/ZrO$_2$ NPs as a fluorescent contrast agent in imaging latent fingerprints (LFPs). (a) Schematic illustration on LFP detection by GNCA/SiO$_2$/ZrO$_2$ NPs. (b) and (c) Photographs of the LFP on the glass substrate before (b) and after (c) adhesion by GNCA/SiO$_2$/ZrO$_2$ NPs under room light. The glass substrate is placed on a piece of black fabric. (d) Photographs of the fingerprint developed by GNCA/SiO$_2$/ZrO$_2$ NPs under UV light at 365 nm, 0.07 mW cm^{-2}. (e$_1$)–(e$_3$) Zoomed-in images of the marked areas on the fingerprint under UV light at 365 nm, 0.07 mW cm^{-2}. (f$_1$)–(f$_3$) Photographs of the LFP on the polystyrene substrate before (f$_1$) and after adhesion by GNCA/SiO$_2$/ZrO$_2$ NPs under room light (f$_2$) and UV light at 365 nm, 0.40 mW cm^{-2} (f$_3$). The transparent substrate is placed on a piece of black fabric. (g$_1$)–(g$_3$) Photographs of the LFP on the aluminum alloy substrate before (g$_1$) and after adhesion by GNCA/SiO$_2$/ZrO$_2$ NPs under room light (g$_2$) and UV light at 365 nm, 0.40 mW cm^{-2} (g$_3$). (h) The LFP pattern developed by GNCA/SiO$_2$ NPs under UV excitation at 365 nm, 0.40 mW cm^{-2}, before (left down) and after (right down) 7 days of storage. (i) The LFP pattern developed by GNCA/SiO$_2$/ZrO$_2$ NPs under UV excitation at 365 nm, 0.07 mW cm^{-2}, before (left down) and after (right down) 7 days of storage.

Conclusions

We report a facile method to encapsulate GNC aggregates obtained from a solvent-induced assembly process into SiO$_2$/ZrO$_2$ NPs. The GNC aggregates give out a strong emission, which are stabilized and rigidified by the inert dual-oxide shell.

Importantly, this synthetic strategy improves both the luminescence and stability of the fluorescent GNCs at the same time, which has always been a great challenge. The zirconia–silica–GNC nanocomposite is found to be a good fluorescent contrast agent in visualizing the latent fingerprints. The oxide shell provides a compatible surface that can easily adhere to

This journal is © The Royal Society of Chemistry 2022

J. Mater. Chem. C, 2022, 10, 10001–10008 | 10007

fingerprint residues on diverse substrates, and the encapsulated GNC aggregates, which emit a bright PL to reveal the morphological details of fingerprints under light excitation. In summary, this work provides an effective way to obtain biofriendly, stable, high-performance metal nanocluster composites, which exhibit promise in various applications such as analysis, illumination, displays and catalysis.

Conflicts of interest

There are no conflicts to declare.

Acknowledgements

References

1   J. Liu, *TrAC, Trends Anal. Chem.*, 2014, **58**, 99.

2   L. Shang, S. Dong and G. U. Nienhaus, *Nano Today*, 2011, **6**, 401.

3   A. Mathew and T. Pradeep, *Part. Part. Syst. Charact.*, 2014, **31**, 1017.

4   H. Kawasaki, H. Yamamoto, H. Fujimori, R. Arakawa, M. Inada and Y. Iwasaki, *Chem. Commun.*, 2010, **46**, 3759.

5   X. Du and R. Jin, *ACS Nano*, 2019, **13**, 7383.

6   R. Jin, Y. Zhu and H. Qian, *Chem. – Eur. J.*, 2011, **17**, 6584.

7   A. Cantelli, G. Guidetti, J. Manzi, V. Caponetti and M. Montalti, *Eur. J. Inorg. Chem.*, 2017, 5068.

8   R. Jin, C. Zeng, M. Zhou and Y. Chen, *Chem. Rev.*, 2016, **116**, 10346.

9   X. Yang, M. Shi, R. Zhou, X. Chen and H. Chen, *Nanoscale*, 2011, **3**, 2596.

10 Z. Luo, X. Yuan, Y. Yu, Q. Zhang, D. T. Leong, J. Y. Lee and J. Xie, *J. Am. Chem. Soc.*, 2012, **134**, 16662.

11 Z. Gan, Y. Lin, L. Luo, G. Han, W. Liu, Z. Liu, C. Yao, L. Weng, L. Liao and J. Chen, *Angew. Chem., Int. Ed.*, 2016, **55**, 11567.

12 R. R. Nasaruddin, T. Chen, N. Yan and J. Xie, *Coord. Chem. Rev.*, 2018, **368**, 60.

13 J. Zheng, C. Zhang and R. M. Dickson, *Phys. Rev. Lett.*, 2004, **93**, 077402.

14 J. Xie, Y. Zheng and J. Y. Ying, *J. Am. Chem. Soc.*, 2009, **131**, 888.

15 X. Le Guével, B. Hötzer, G. Jung and M. Schneider, *J. Mater. Chem.*, 2011, **21**, 2974.

16 G. De Cremer, B. F. Sels, J. Hotta, M. B. Roeffaers, E. Bartholomeeusen, E. Coutiño-Gonzalez, V. Valtchev, D. E. De Vos, T. Vosch and J. Hofkens, *Adv. Mater.*, 2010, **22**, 957.

17 A. Royon, K. Bourhis, M. Bellec, G. Papon, B. Bousquet, Y. Deshayes, T. Cardinal and L. Canioni, *Adv. Mater.*, 2010, **22**, 5282.

18 M. R. Narouz, K. M. Osten, P. J. Unsworth, R. W. Y. Man, K. Salorinne, S. Takano, R. Tomihara, S. Kaappa, S. Malola, C.-T. Dinh, J. D. Padmos, K. Ayoo, P. J. Garrett, M. Nambo, J. H. Horton, E. H. Sargent, H. Häkkinen, T. Tsukuda and C. M. Crudden, *Nat. Chem.*, 2019, **11**, 419.

19 F. Zhang, Z.-F. Shi, Z.-Z. Ma, Y. Li, S. Li, D. Wu, T.-T. Xu, X.-J. Li, C.-X. Shan and G.-T. Du, *Nanoscale*, 2018, **10**, 20131.

20 X. Li, W. Cai, H. Guan, S. Zhao, S. Cao, C. Chen, M. Liu and Z. Zang, *Chem. Eng. J.*, 2021, **419**, 129551.

21 K. Pyo, V. D. Thanthirige, K. Kwak, P. Pandurangan, G. Ramakrishna and D. Lee, *J. Am. Chem. Soc.*, 2015, **137**, 8244–8250.

22 X. Le Guével, C. Spies, N. Daum, G. Jung and M. Schneider, *Nano Res.*, 2012, **5**, 379.

23 X. Wu, L. Li, L. Zhang, T. Wang, C. Wang and Z. Su, *J. Mater. Chem. B*, 2015, **3**, 2421.

24 T. Kim, H. Jang, S. Kim, J.-H. Lee, S.-Y. Kim, N. L. Jeon, J. M. Song and D.-H. Min, *Langmuir*, 2018, **34**, 173.

25 S. Zhang, R. Liu, Q. Cui, Y. Yang, Q. Cao, W. Xu and L. Li, *ACS Appl. Mater. Interfaces*, 2017, **9**, 44134.

26 Z. Soran-Erdem, T. Erdem, K. Gungor, J. Pennakalathil, D. Tuncel and H. V. Demir, *ACS Nano*, 2016, **10**, 5333.

27 P. Hazarika, S. M. Jickells, K. Wolff and D. A. Russell, *Angew. Chem., Int. Ed.*, 2008, **47**, 10167.

28 X. Gao, Y. Lu, M. Liu, S. He and W. Chen, *J. Mater. Chem. C*, 2015, **3**, 4050.

29 K. Zheng, X. Yuan, K. Kuah, Z. Luo, Q. Yao, Q. Zhang and J. Xie, *Chem. Commun.*, 2015, **51**, 15165.

30 Z. Wang, B. Chen, M. Zhu, S. V. Kershaw, C. Zhi, H. Zhong and A. L. Rogach, *ACS Appl. Mater. Interfaces*, 2016, **8**, 33993.

31 J. Lee, *Macromol. Biosci.*, 2005, **5**, 1085.

32 Z. Wu and R. Jin, *Nano Lett.*, 2010, **10**, 2568.

33 A. Haugeneder, U. Lemmer and U. Scherf, *Chem. Phys. Lett.*, 2002, **351**, 354.

34 J. Gierschner, H.-J. Egelhaaf, D. Oelkrug and K. Müllen, *J. Fluoresc.*, 1998, **8**, 37.

35 M. Wu, J. Zhao, D. M. Chevrier, P. Zhang and L. Liu, *J. Phys. Chem. C*, 2019, **123**, 6010.

36 X. Jia, J. Li and E. Wang, *Small*, 2013, **9**, 3873.

37 Q. Li, M. Zhou, W. Y. So, J. Huang, M. Li, D. R. Kauffman, M. Cotlet, T. Higaki, L. A. Peteanu, Z. Shao and R. Jin, *J. Am. Chem. Soc.*, 2019, **141**, 5314.

38 Y. Yusof and M. R. Johan, *CrystEngComm*, 2014, **16**, 8570.

39 S. Mallick, S. Rana and K. Parida, *Dalton Trans.*, 2011, **40**, 9169.

40 K. Gurushantha, K. S. Anantharaju, L. Renuka, S. C. Sharma, H. P. Nagaswarupa, S. C. Prashantha, Y. S. Vidya and H. Nagabhushana, *RSC Adv.*, 2017, 7, 12690.

41 D. Maltoni, D. Maio, A. K. Jain and S. Prabhakar, *Handbook of fingerprint recognition*, Springer Science & Business Media, 2009.

10008 | *J. Mater. Chem. C*, 2022, **10**, 10001–10008

This journal is © The Royal Society of Chemistry 2022